Investigation of Local Structure and Enhanced Thermal Stability of Ir-doped PdRu Nanoparticles for Three-way Catalytic Application[†]

Akhil Tayal,[*,†,‡] Okkyun Seo,[‡,⊥] Jaemyung Kim,[‡] Kohei Kusada,[¶] Hiroshi Kitagawa,[¶] and Osami Sakata[*,‡,§,‖]

†*Deutsches Elektronen-Synchrotron, Notkestrasse 85, Hamburg 22607, Germany.*

‡*Synchrotron X-ray Group, Research Center for Advanced Measurement and Characterization, National Institute for Materials Science, 1-1-1 Kouto, Sayo, Hyogo 679-5148, Japan.*

¶*Division of Chemistry, Graduate School of Science, Kyoto University, Kitashirakawa Oiwake-cho, Sakyo-ku, Kyoto 606-8502, Japan.*

§*Department of Materials Science and Engineering, Tokyo Institute of Technology, Nagatsuta, Midori, Yokohama 226-8502, Japan.*

‖*Center for Synchrotron Radiation Research, Japan Synchrotron Radiation Research Institute (JASRI), 1-1-1 Kouto, Sayo, Hyogo 679-5198, Japan.*

⊥*Contributed equally to this work*

E-mail: akhil.tayal@desy.de; SAKATA.Osami@nims.go.jp,sakata.osami@spring8.or.jp

Abstract

The local structure and thermal stability of newly synthesized PdRuIr and PdRu alloy nanoparticles (NPs) were studied using X-ray absorption fine structure spectroscopy

(XAFS) and compared with those of Ru NPs. Pd K-edge XAFS reveals that a significant fraction of Pd segregates, forming metal NP clusters. In the PdRuIr NPs, a small fraction of Pd forms an alloy with Ir, whereas a majority phase is Ru-Ir alloy having the novel face-centered cubic structure. Apart from the distinct local surroundings, XAFS analysis revealed the presence of an anharmonic disorder in the PdRu and PdRuIr NPs. The previously observed enhanced thermal stability with Pd and Ir doping was investigated using temperature-dependent $in-situ$ XAFS. In the Ru NPs, an abrupt change in the near-edge features was observed at 673 K, which was gradually suppressed for PdRu and PdRuIr NPs. At this temperature, the dynamical fluctuations were more pronounced in the pure Ru NPs, helping to convert surface-adsorbed O_2 into the volatile RuO_4 phase, thereby leading to earlier evaporation of Ru. Dynamical fluctuation suppresses with alloying elements or gets extended to a higher temperature, helping to delay the RuO_4 formation process and enhancing the thermal stability of the PdRu and PdRuIr NPs in increasing order.

Introduction

Ruthenium (Ru) nanoparticles (NPs) are known to display excellent catalytic properties for the oxidation of CO/hydrocarbons and NO_x reduction.[1–5] Recently, numerous investigations have been devoted to enhancing the catalytic performance of Ru NPs.[6] It has been demonstrated that the catalytic properties of bimetallic alloys such as PdRu show drastic improvement in CO oxidation capability relative to individual Pd/Ru NPs.[7–9] Although Pd and Ru are an immiscible system in bulk form, solid-solution alloy NPs form because of the distinct thermodynamics activity in the NP state.[10] PdRu alloy NPs can be synthesized over a wide composition range with the catalytic properties varying with the composition.[7] The observed enhanced catalytic features provide an opportunity to explore immiscible metal alloy NPs and understand the effect of the underlying microstructures and electronic properties on their unique catalytic properties.[9,11] In addition, it paves a path for the use of the catalytic properties of Pd in the bimetallic alloy configuration, which is known for its use in a variety of catalytic applications such as hydrogen storage .[12,13] Consequently, the bimetallic alloy of PdRu has been shown to be very useful for three-way catalytic (TWC) applications.

Despite their marked improvement for TWC applications, PdRu alloy NPs suffer from one significant drawback. The performance of these composites deteriorates in real-world application in exhaust systems because of the high operating temperatures (373 K–873 K). Even at moderate temperature, the critical component Ru is evaporated by converting into the highly volatile RuO_4, preventing the full utilization of the bimetallic functionality for TWC applications. Consequently, it has been proposed that the addition of a third element such as Ir could significantly enhance the thermal stability of the PdRu system without adversely affecting the TWC properties.[14,15] Moreover, structural analysis was carried out using XRD, revealing that the ternary alloy sample mainly crystalizes in the fcc structure.[14,15]

Interestingly, PdRu and PdIr are immiscible in bulk form, and alloy formation is only facilitated in NPs. Therefore, apart from the challenges involved in synthesizing such ternary hybrid catalysts, several issues related to their structural and electronic properties must be systematically investigated if they are foreseen to replace monometallic or bimetallic alloy NPs. Consequently, investigation of the structure of these alloys to address their effect on the stability and useful catalytic properties is necessary. In earlier reports, it was observed that the microstructure and size of NPs have a substantial effect on the catalytic properties.[3,10,16–19] In the bulk immiscible systems, because of unfavorable thermodynamics, the formation of metastable structures can produce disorder and inhomogeneity in the sample. The inhomogeneity can lead to compositional disorder or/and the formation of metal clusters of different sizes.[9,11] As the catalytic properties are known to be affected by the size of the NPs, it is necessary to probe the microstructure in such a ternary alloy system. Moreover, owing to possible alloying and hybridization of electronic states, unusual electronic properties emerge, which may correlate with the microstructure. Therefore, the local structure can provide crucial insight on the functioning of these novel catalysts.

As these ternary systems are affected by these limitations, it is imperative to understand how the addition of any immiscible element in the already metastable alloy leads to enhancement of the thermal stability. Therefore, the present investigation is devoted to shedding light on the following aspects. The first is to investigate the local structure of Ru, Pd, and Ir and observe whether they form a ternary alloy or whether any segregation occurs in the NP state owing to their immiscible nature. Later, the thermal stability of the ternary alloy system is reported, and the results are compared with that of monometallic Ru NPs and bimetallic PdRu NP to obtain different dynamical parameters that govern the stability of these systems. We propose the mechanism of the earlier evaporation or suppression of Ru with and without the alloying elements.

The XAFS technique can effectively probe the local structure because of its elemental sensitivity, which is advantageous for examining the local surrounding of alloying elements. In this report, we discuss XAFS measurements performed at the Ru K-edge, Pd K-edge, and Ir L_3-edge. The XAFS measurements on the as-prepared samples provide crucial insight on the subtle variation in the local structure of the bimetallic and ternary NP alloy system. The NP samples of Ru, PdRu, and PdRuIr were heated from ambient temperature to 1273 K to investigate the process of Ru evaporation in pure Ru NPs and compare the effect in the presence of different alloying elements. The observed variation in the local structure and valence state suggest the role of dynamical fluctuation and alloying in the evaporation process of Ru in the bimetallic and ternary alloy NPs.

Methods

XAFS spectra on all the samples were measured at the BL01B1 beamline at SPring-8, Japan. A Si(311) double-crystal monochromator was used to monochromatize the beam, and energy scans were performed near the Pd K-edge, Ru K-edge, and Ir L_3-edge. The calibration of the monochromator was monitored by measuring multiple XAFS spectra on metal references (Ru, Pd, and Ir) during the experiment and found to be not varied throughout the entire experiment. The nanoparticle samples were placed in a 1-mm-diameter quartz capillary tube, and XAFS measurements were performed in transmission mode. The capillary was placed in the oven with the Kapton window in the beam path. The samples were radiatively heated from ambient temperature to 1000 °C (1273 K) in the vacuum furnace with a base pressure on the order of 10^{-2} mbar. The sample environment was evacuated to allow only partial oxidation of Ru to precisely investigate the mechanism of thermal stability. The XAFS spectra at each edge were collected at different temperatures after allowing the sample to equilibrate for 10 min at each temperature. The temperature was ramped up at a rate of 20 K/min. The total time for the measurement at one edge was approximately 20 min, and the XAFS measurements at all the edges were completed in 90 min. The pre-edge and post-edge background subtraction of the data was performed following the standard procedure in Athena software.[20,21] The $\chi(k)$ extended X-ray absorption fine structure spectroscopy (EXAFS) signal was extracted by subtracting a background absorption function. The polynomial spline function was estimated by connecting various third-order polynomial functions over several positions called knots (3/4) in the k-space. Later, the positions of knots were varied to suppress the amplitude of the Fourier-transform modulus between 0 and 1 Å.[21] A computer program written by Conradson *et al.*[22] was used to perform the EXAFS fitting. The NPs are prepared by chemical reduction method (see Supplementary information).

Results & Discussion

In the solid-solution alloy, the alloying atoms are substituted in the solute crystal, and the final crystallographic phase is determined by the equilibrium free energy.[23] The structure of the final phase also depends on the solute concentration. At lower concentration, the initial crystallographic structure of the solute can be retained with either partial or no modification

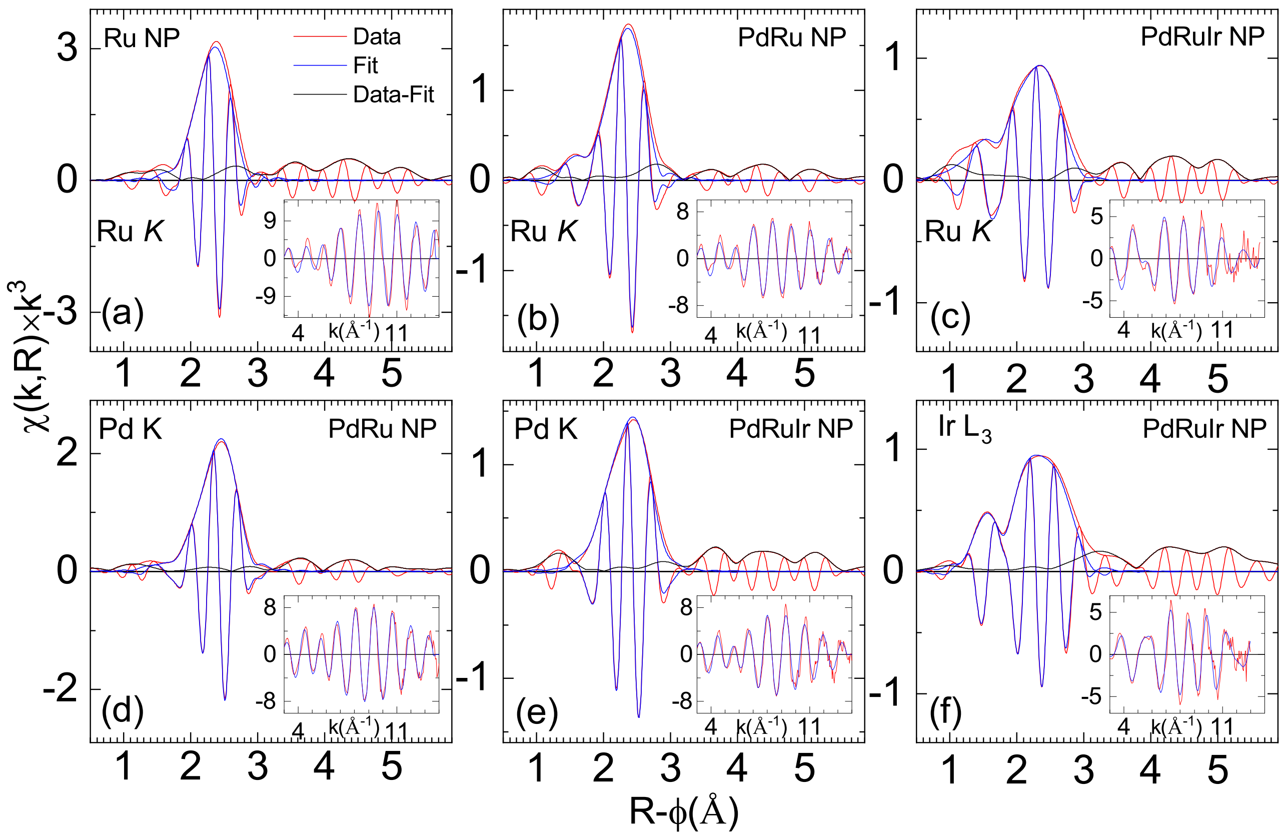

Figure 1: $\chi(\mathrm{k})\times\mathrm{k}^3$ EXAFS of Ru NPs (a), PdRu NPs (d,e) and PdRuIr NPs (c,e,f) measured at Ru K-edge(a-c), Pd K-edge(d,e) and Ir L_3-edge (f). FT modulus and real part of data and fit are shown with inset showing corresponding $\chi(\mathrm{k})\times\mathrm{k}^3$ data and fit.

of the crystallographic parameters. Higher concentration can convert the structure into a new crystallographic phase or heterogeneous structure.[24] These sets of protocols, which are normally attributed to bulk alloys, often break for nanosized systems.[25] In the NPs, one can vary the composition over a wide range and obtain novel crystallographic structures.[7,26] Therefore, various parameters need to be considered beforehand to avoid any ambiguity in the analysis of the local structure of the ternary alloy NPs.

The bulk crystallographic structure of Ru is hexagonal close packed (hcp), whereas Pd and Ir crystallize in the fcc structure with first atomic pair distances in the Ru, Pd, and Ir lattices of 2.66 Å, 2.75 Å, and 2.71 Å, respectively. The PdRu NPs are an equiatomic alloy with 50:50 composition, whereas in the PdRuIr NPs, each element is present as one-third of the composition. Although the atomic composition in PdRu alloy is similar, both the elements have different bulk crystallographic structures. Therefore, the final alloy phase can have either an fcc or a hcp structure. No alternative structure of PdRu alloy NPs has been reported.[7,26] However, for PdRuIr NPs, two-thirds of the composition is made up of the elements Pd and Ir with the fcc structure and similar lattice parameters; therefore, the alloy preferably crystallizes into the fcc structure. Recently, it was demonstrated that Ru can crystallize into the fcc structure in the NPs and shows superior catalytic properties.[26] For Pd, Ru, and Ir, as the interatomic distance is quite similar, no significant variation in the interatomic distance is expected in the substitutionally dissolved solid-solution alloy phase. In addition, the resolution limit for EXAFS to estimate the change in the atomic pair distance is approximately 0.02 Å. In the presence of any anharmonic disorder, the size distribution of NPs, compositional disorder, any distinction among the closely separated shell becomes extremely challenging to determine from EXAFS analysis. One additional caveat is the photoelectron backscattering amplitude, which is similar for Ru and Pd because of their similar atomic numbers.[27] Consequently, one cannot distinguish the Ru–Pd atomic pairs in the alloys. However, the atomic number and photoelectron backscattering amplitude of Ir are very different from those of Pd and Ru, facilitating distinguishing between Pd–Ir and Ru–Ir atomic pairs.

In the first attempt to identify the nature of alloying in the PdRuIr NPs and compare it with that of the Ru and PdRu NPs, a first-shell fit of the EXAFS data was performed on the spectra measured at the Ru K-edge, Pd K-edge, and Ir L_3-edge under ambient condition. Fig. 1 presents the fitted EXAFS spectra of the indicated samples, and the obtained metrical parameters are tabulated in Table 1. For the Ru NPs (Fig. 1(a)), the first FT peak is composed of Ru–Ru atomic pairs at 2.66 Å and 2.70 Å; however, given the very close separation, a single shell fit with the average value of these two shells can be used to fit the $\chi(k)$ data. Using this approach, the Ru–Ru atomic pair distance for the Ru NPs was determined to be 2.66 Å as compared with the value obtained for the Ru foil of 2.68 Å. A slightly smaller interatomic shell distance for the NPs is expected because of the contribution from the surface atomic pairs with a distinct atomic pair distance compared with that of the bulk.[28,29] For the PdRu NPs (Fig. 1(b)), as the Ru–Pd atomic pairs could not be distinguished, a single shell fit gave a Ru–Ru shell distance of 2.66 Å. The FT spectrum for the PdRuIr alloys (Fig. 1(c)) was distinct from those for the Ru and PdRu NPs, with a broad FT peak in the region between 1.9 and 3 Å . Using this single shell fitting approach, a significant amount of unfitted residual component was observed in the EXAFS fit. Inclusion of the Ru–Ir shell improved the quality of the fit and reduced the χ^2 (goodness of fit) value significantly. The presence of the Ru–Ir shell indicates that Ir formed a solid-solution alloy with Ru. As the Ru–Pd pairs were not distinguishable, the presence of PdRuIr alloy in the sample cannot be ruled out. In addition, the presence of FT amplitude near the 1.6 Å region (Fig. 1(b), (c), and (f)) indicates some surface adsorption of PVP to the NPs which was included in the fit as a metal-oxide shell ($\approx$1.98±0.02 Å) and found to have coordination number between 0.2–1.

Table 1: Metrical parameters such as atomic pair distance (R (Å)), coordination number (N), root-mean-square displacement (σ (Å)), and edge shift between experimental and theoretical EXAFS (ΔE_0 (eV)) are obtained from the EXAFS fitting.

Parameters	Ru NPs	PdRu NPs	PdRu NPs	PdRuIr NPs		PdRuIr NPs		PdRuIr NPs	
	Ru K	Ru K	Pd K	Ru K		Pd K		Ir L_3	
	Ru-Ru	Ru-Ru	Pd-Pd	Ru-Ru	Ru-Ir	Pd-Pd	Pd-Ir	Ir-Ir	Ir-Ru
R(Å)	2.66±0.01	2.66±0.01	2.71±0.01	2.68±0.01	2.68±0.01	2.71±0.01	2.70±0.01	2.67±0.01	2.67±0.01
N	7.6±1.8	6.7±1.5	9.0±1.9	4.0±0.9	1.5±0.4	6.0±1.4	2.8±0.8	4.3±1.0	2.6±0.6
σ	0.07±0.01	0.08±0.01	0.09±0.01	0.07±0.01	0.06±0.01	0.08±0.01	0.08±0.01	0.06±0.01	0.05±0.01
ΔE_0	-0.7±3	-1.2±2.5	-2.2±2.3	-0.1±3.4	0.9±4.3	-2.2±2.7	-3.2±4.4	-1.5±3.6	-2.5±3.5

The FT spectra of the PdRu NPs (Fig. 1(d)) and PdRuIr NPs (Fig. 1(e)) at the Pd K-edge show an intense peak at 2.2 Å , which was fitted with the single Pd–Pd shell. However, for the PdRuIr NPs, a comparison of the $\chi(R)$ spectra with those of the PdRu NPs (Fig. S1) reveals that the node positions in the real component spectra are not similar. This trend was also observed in the $\chi(k)$ (Fig. S1) data, indicating the distinct local structure of Pd in both samples. For the PdRuIr NPs, inclusion of the Pd–Ir shell resulted in a marginal improvement in the quality of fit. This finding indicates that only a small fraction of Ir was present in the local surrounding of Pd and that a significant fraction of Pd may become segregated in the form of Pd or PdRu NP clusters. The Pd–Pd and Pd–Ir shell distance was ≈2.7 Å , which is slightly higher than that of the Ru–Ru/Ru–Ir shells (Table 1). Therefore, the Pd K-edge data suggest that if some fraction of the sample contains PdRu as an alloy phase, it has an atomic pair distance similar to that of fcc Pd as Pd–Ru shells cannot be distinguished in the EXAFS. Another possibility is that PdIr has formed isolated clusters in the sample.

The FT spectrum measured at the Ir L_3-edge (Fig. 1(f)) possessed similar features as those at the Ru K-edge. The broad first peak could be fitted with two shells (Ir–Ir and Ir–Ru). The obtained atomic pair distances were similar to those obtained at the Ru K-edge (Table 1), suggesting that a significant fraction of Ir had formed an alloy with Ru. As the fraction of the Ir–Pd alloy phase was relatively small and the Ru and Pd EXAFS signal overlapped, any attempt to fit the data with an additional Ir–Pd shell would not be convincing. Therefore, the above analysis indicates that the ternary alloy contained the Ru–Ir alloy, isolated Pd/PdRu clusters, and a small fraction of the Pd–Ir alloy phase. Given that Ir surrounded both Pd and Ru and the limitation of the EXAFS technique to distinguish between these two elements, the possibility of the formation of PdRuIr in the sample cannot be completely ruled out.

The EXAFS fitting at different edges revealed nearly similar atomic pair distances, making it difficult to obtain information on the possible crystallographic structure. Moreover, Ru and Ir had distinct bulk structures but showed similar atomic pair distances in the alloy NPs. Therefore, to obtain more information on the crystallographic phase of the PdRuIr NPs, further analysis was performed. The use of continuous Cauchy wavelet (CCW) analysis to distinguish between different elements has been proposed.[30] Such analysis provides a three-dimensional visualization of the wave vector $\chi(k)$, the phase-shift-uncorrected interatomic distance, and CCW transform (CCWT) modulus space. The applicability of this method arises because of the variation in the photoelectron backscattering amplitude for different elements and its dependence on the wave vector. The $\chi(\mathrm{k})$ amplitude decayed relatively more slowly in the high-k region for scattering elements with a higher atomic number. This approach can thus be helpful in distinguishing among closely spaced atomic pairs consisting of elements with a significant difference (±10) in atomic number.[27] Fig. S2 presents the CCWT of Ru NPs at the Ru K-edge (a) and PdRu NPs at the Ru K-edge (b) and Pd K-edge (c). The single ridge of the CCWT modulus was attributed to the overlapping first and second coordination shells in the hcp Ru at 2.66 Å and 2.70 Å, respectively. Similar features can be seen for the PdRu NPs measured at the Ru K-edge and Pd K-edge. These spectra are compared with Ru and Pd references in which the CCWT ridge appears at approximately $9.5\,\text{Å}^{-1}$ (Fig. S3) for both samples. For the Ru NPs, the ridge in the k-space falls at a similar position as that observed for the bulk. However, for the PdRu NPs, the ridge positions for the spectra measured at the Ru K and Pd K-edges were at $8.7\,\text{Å}^{-1}$ and $8.9\,\text{Å}^{-1}$, respectively. These results indicate that specific crystallographic disorder is present in the sample, which causes the rapid decay of χ(k) in the high-k region and could stem from alloying. Fig. 2 presents the CCWT spectra measured at the Ru K-edge (a,b) and Ir L_3-edge(c,d) for the Ru reference (a), Ir reference (b), and PdRuIr NPs (c,d). For the Ru reference, a single ridge feature was present; however, for the Ir reference, two ridge features at approximately $10.1\,\text{Å}^{-1}$ are present. The first feature is attributed to the first Ir–Ir shell at the distance of 2.71 Å and the second feature at 4 Å can be attributed to the multiple scattering paths with amplitudes that become significantly enhanced in the fcc structure owing to the focusing effect.[21] In the CCWT spectrum measured at the Ru K-edge and Ir L_3-edge, the signature of these features was present. Furthermore, the FT modulus of the Ru K-edge (Fig. 2(c)) and Ir L_3-edge (Fig. 2(d)) for the PdRuIr samples are split in two peaks near the first coordination region as compared to the FT modulus of the corresponding reference samples. These observations indicate that for the PdRuIr system, Ir–Ru is forming a solid solution that that could have a long-range fcc structure similar to that of Ir. However, as distinction between Ru and Pd is not possible, the formation of a complex solid solution of Pd–Ru with Ir cannot be ruled out. Moreover, the X-ray diffraction results in Fig. S4 confirm the formation of a fcc structure for the PdRuIr alloy NPs. Since elements with a close atomic number are difficult to distinguish with XAFS and XRD, the anomalous scattering approach might provide better information on the size, shape, and spatial distribution of Ru/Pd in the nanoparticles.[31]

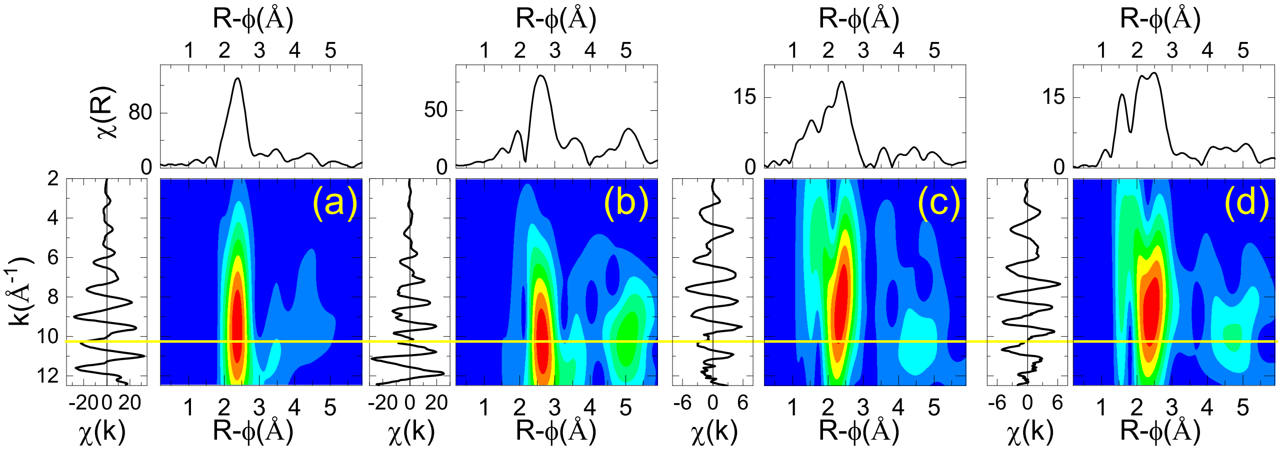

Figure 2: CCWT, χ(k), and Fourier transform spectra of Ru reference (a), Ir reference (b) and PdRuIr NP (c,d) NPs measured at Ru K-edge (a,c) and Ir L_3-edge (b,d). The yellow line is placed at the WT ridge (10.2 Å^{-1}) for Ir reference(b) to compare other samples.

In the next section, the thermal stability of the Ru NPs, PdRu NPs, and PdRuIr NPs was investigated. Earlier, the evaporation of ruthenium was observed to be significantly affected by the alloying elements. In the Ru NPs, the evaporation of Ru was much faster and occurred at a moderate temperature of approximately 673 K (400 °C). For the PdRu system, the Ru evaporation was limited; however, for the ternary alloy system PdRuIr, the evaporation of Ru was remarkably suppressed. In the present analysis, we try to understand the mechanism for the thermal instability in the Ru NPs and the stability in the bimetallic and ternary alloy NPs to shed light on the mechanism affecting their thermal stability.

Fig. S5 presents a XANES profile of the Ru K-edge for the Ru NPs, PdRu NPs, and PdRuIr NPs measured at different temperatures up to 1273 K (1000 °C). The near-edge features after the white line at approximately 22155 eV for the Ru K-edge and 24385 eV for the Pd K-edge are marked by '*C*'. The intensity of this feature was found to correlate with the oxide formation at the NP surface.[32–34] In general, it was observed that the for the RuO_2

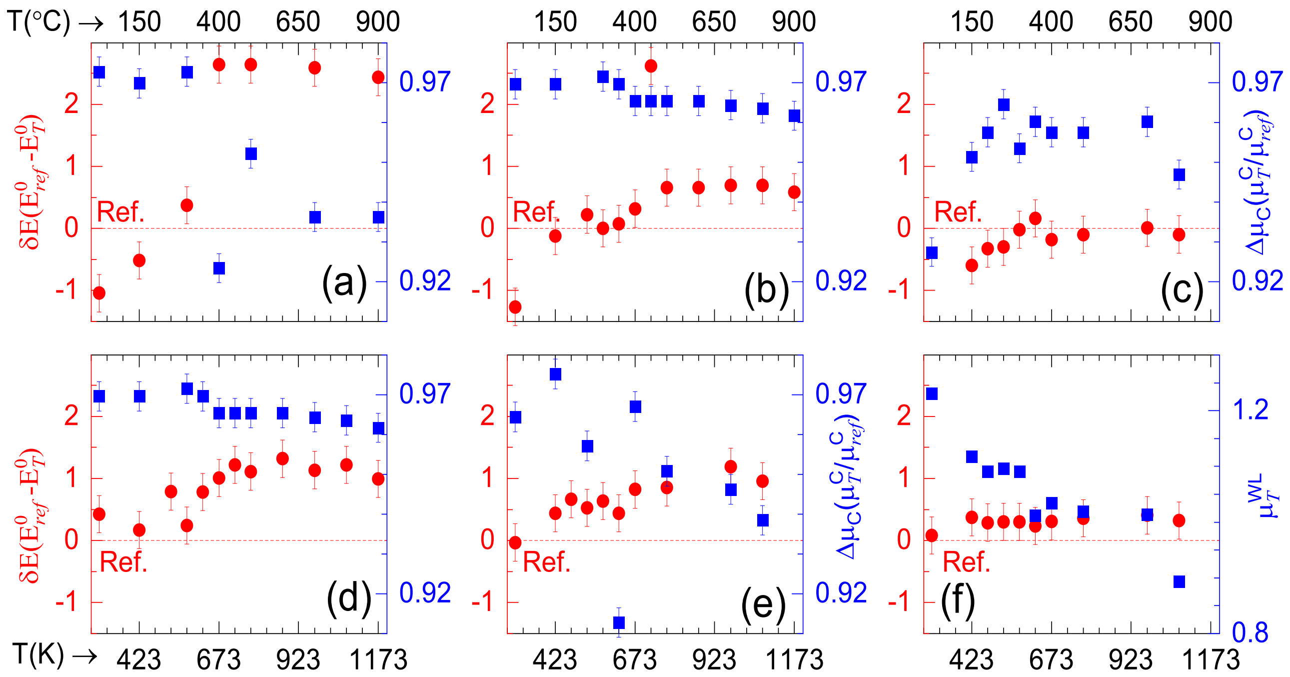

Figure 3: Difference between edge position measured at different temperature with the reference (red solid circles) and ratio of intensity of feature C with reference (blue solid rectangles) for the spectra measured at the Ru K-edge (a,b,c), Pd K-edge (d,e) and Ir L_3-edge (f) for the Ru NP (a), PdRu NPs (b,d) and PdRuIr NPs (c,e,f). In figure (f) variation in the white line intensity is plotted instead of feature 'C'.

or PdO, the feature C had significantly lower intensity than those of the metallic Ru/Pd;[34,35] therefore it can act as a good indicator to observe the variation in the surface state of NPs with temperature. Fig. 3 shows the shift in the edge position relative to the respective bulk reference measured at ambient temperature (shown as red filled circles) and the intensity of the feature 'C' normalized to that the same feature observed in the respective bulk (blue solid rectangles) at different temperatures. It can be seen that for the pure Ru NPs (Fig. 3(a)), after 673 K (400 °C), there was a sudden variation in the edge position and the intensity of feature 'C'. These variations were quite substantial relative to those for the PdRu or PdRuIr samples, which will be discussed later. Interestingly, a red-shift toward lower energy in the edge position was observed relative to the bulk Ru with increasing temperature. Such drastic variation in the edge position and the relative intensity of the feature 'C' were not observed with the Pd/Ir alloying elements (Fig. 3(b,c)). For the PdRu NPs (Fig. 3(b)), the red-shift was marginal, and similar variation was observed in the intensity of the feature 'C'. Interestingly, for the PdRuIr NPs (Fig. 3(c)), no red-shift was apparent. The edge position remained stable with temperature and had a higher value relative to that of the Ru reference. The intensity of the feature 'C' followed a similar trend. These results indicate that the thermal instability in Ru is likely to occur at and above 673 K (400 °C) and that the alloying elements somehow retarded it, thus improving the stability of the systems.

Comparing the behavior with that of other alloying elements, one can see that for the spectrum measured at the Pd K-edge (Fig. 3(d)), the trend in the edge position is similar for the PdRu NPs, as observed for Ru K-edge. For the Pd K-edge XAFS measured on the PdRuIr NPs (Fig. 3(e)), the red-shift was still apparent; however, the intensity of the feature 'C' showed a decreasing trend with temperature. This finding indicates that the Pd acts independently compared with Ru in the PdRuIr NPs, which supports the hypothesis that a significant fraction of Pd is segregated in the PdRuIr NPs, as discussed earlier. For the Ir L_3-XAFS (Fig. 3(f)), the white line intensity was compared instead of the feature 'C', indicating the number of *d*-holes, and can be correlated with the formation of oxide. The edge position remained similar to the bulk value. The white line intensity showed some decrease above 423 K (150 °C), which can be attributed to the desorption of PVP from the NP surface. Between 423 K and 1073 K, it remained stable with only a slight decrease above 673 K followed by a rapid decrease at approximately 1073 K. These results indicate that the behavior of Ir is similar to that observed for the Ru and that any suppression of Ru evaporation can be attributed to the formation of an alloy with Ir.

To understand the observed behavior of enhanced thermal stability in the presence of Ir, we considered the role of dynamical fluctuations. In an earlier investigation by Vila *et al.* on Pt NPs supported on Al_2O_3, it was observed both experimentally and using density functional theoretical simulation that the Pt L_3-edge shows a red-shift at 473 K relative to the spectrum measured at 167 K.[36] These results are explained in terms of dynamical fluctuation that arises from the combined effects of nanoparticle charging, chemical shift, and entropic effect.[36] Using this model, the observed results can be explained to understand the suppression of Ru evaporation with the alloying elements. It can be deduced that for the Ru NPs, because of the high dynamical fluctuation, the surface of the NPs is highly active, facilitating the formation of volatile RuO_4 via conversion of the surface oxide phase formed with the adsorbed O_2. The highly active NP surface could lead to the conversion of the Ru NPs to RuO_2 to RuO_4 that causes the earlier evaporation of Ru in the monometallic state. For the PdRu system, because it is an immiscible system, the formation of an alloy in the nanoparticle state is facilitated only by structural disorder. It was observed that with increasing temperature, the Pd and Ru can become segregated. Therefore, the adsorbed O_2 on the NPs interacts differently with monometallic clusters of Ru, Pd and the bimetallic fraction of PdRu, which can result in a reduction of the dynamical fluctuation compared with that of monometallic Ru. However, the suppression was not sufficient for the PdRu system to significantly delay the evaporation of Ru. With the inclusion of third elements and the formation of an alloy phase with Ru, the effect of dynamical fluctuation was significantly reduced in the Ru(Pd)Ir alloy, which can retard the formation of RuO_4, resulting in the suppression of Ru evaporation. It can be postulated that the negative shift in the edge position results from the nanoparticle charging. Thus, charged NPs could serve as active sites for converting surface ruthenium oxide to the volatile RuO_4. Additionally, the coverage of such sites could be higher in the monometallic NPs, accelerating further oxidation of Ru. However, a detailed surface study is required to understand the exact behavior of dynamical fluctuation.

Fig. 4 presents the FT spectra of the indicated samples measured at the Ru K-edge, Pd K-edge, and Ir L_3-edge at different temperatures. For the spectra measured at the Ru K-edge(a-c), Pd K-edge(d,e), and Ir L_3-edge (f) for the Ru NPs (a), PdRu NPs (b,d) and PdRuIr NPs (c,e,f) a common observation was that the intensity of the first FT peak decreased with increasing temperature. At sufficiently high temperature of approximately 673 K, the amplitude in the higher-R region above 3 Å was suppressed significantly relative to

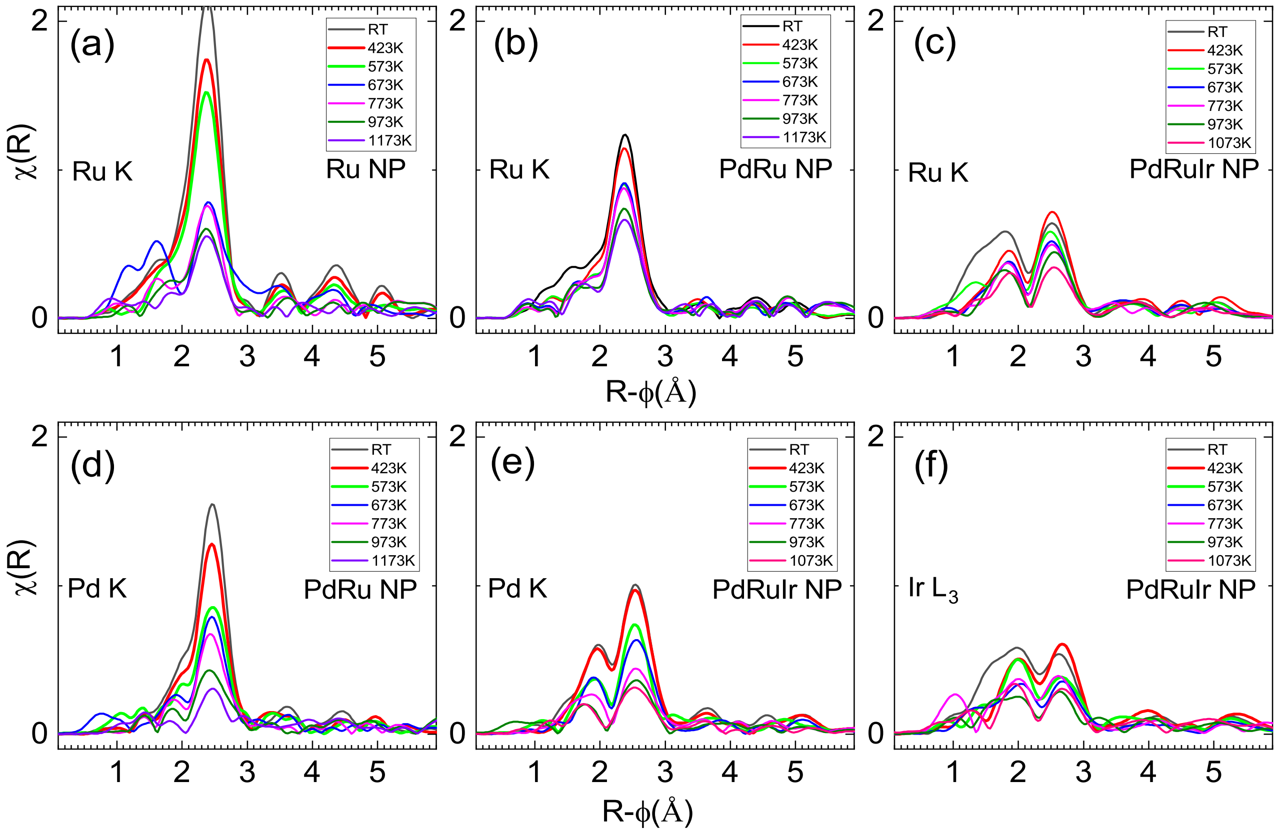

Figure 4: FT spectra of samples measured at Ru K-edge (a,b,c), Pd K-edge (d,e) and Ir L_3-edge (f) for the Ru NP (a), PdRu NPs (b,d) and PdRuIr NPs (c,e,f) at difference temperatures.

the FT intensity of the first peak. This result suggests that the higher-order shells are highly affected by thermal disorder, tailing off their $\chi(k)$ signal. For the Ru NPs, the magnitude of the FT peak slightly decreased up to 573 K with an abrupt decrease after 673 K. For the PdRu NPs, the FT amplitude gradually decreased up to 423 K. However, the decrease was not abrupt as observed for the Ru NPs. The situation was further improved for the PdRuIr NPs, where a gradual reduction of the FT peak intensity was observed with no sign of an abrupt change as for the Ru/PdRu NPs. This behavior was also observed in the spectra measured at the Pd K-edge for the PdRu NPs and PdRuIr NPs. For the PdRu and PdRuIr NPs, the FT peak amplitude after 573 K gradually decreased. Similarly, a non-abrupt decrease in FT amplitude with temperature was observed in the FT spectra measured at the Ir L_3-edge.

The amplitude of an FT peak is known to be correlated with the coordination number and

Debye–Waller factor, both of which can contribute to the decrease in the FT peak intensity. With increasing temperature, the Debye–Waller factor becomes larger, inevitably resulted in a decrease of the FT amplitude. However, evaporation of Ru from the NP surface would reduce the size of the NPs, which can also result in the decrease of the coordination number with temperature. Therefore, the observed decrease in the FT amplitude can be attributed to the combined effect of the enhanced Debye–Waller factor with temperature and/or the decrease in the coordination number with the evaporation of Ru.

Because the coordination number and Debye–Waller factor are highly correlated, it is difficult to separate the effects of these parameters on the FT amplitude. Additionally, the FT amplitude is also correlated with the anharmonicity and compositional disorder, among other properties.[28,37] In addition, in stable metal NP alloys, a distribution in the cluster size can also affect the FT amplitude. In the absence of sufficient fitting constraints, any EXAFS modeling can give erroneous results. However, an alternative approach using ratios can provide a more directed representation of the disorder and coordination number on the FT amplitude.[38,39] In this approach, the $\chi(k)$ data of the first shell is isolated from that of the rest of the shells. Later, by performing Fourier back transform, the $\chi(k)$ amplitude and corresponding phase can be determined. The logarithm ratio of the $\chi(k)$ amplitude measured at different temperatures with the $\chi(k)$ amplitude measured at ambient temperature is plotted against k^2. Similarly, the difference of phases is plotted against k. Bunker [38]proposed that the amplitude and phase graphs can be fitted with the following equations to obtain information on the relative variation of different parameters of the equation with the model spectrum.

$$Log - Ratio(k) = c_0 + 2c_2k^2 + \frac{2}{3}c_4k^4$$

$$Phase - Difference(k) = 2c_1k - \frac{4}{3}c_3k^3$$

Here, c_0, c_1, c_2, c_3, and c_4 are zero to fourth-order cumulants.[40] c_1 gives information on the variation in the atomic pair distance; c_2 is σ; and c_3 and c_4 are related to the anharmonicity in the samples, which affects the phase and amplitude, respectively. If the anharmonicity and disorder are assumed to be constant, the log-ratio curve is a straight line when plotted against k^2. The slope of this line is related to the Debye–Waller factor, and the intercept is related to the coordination number.

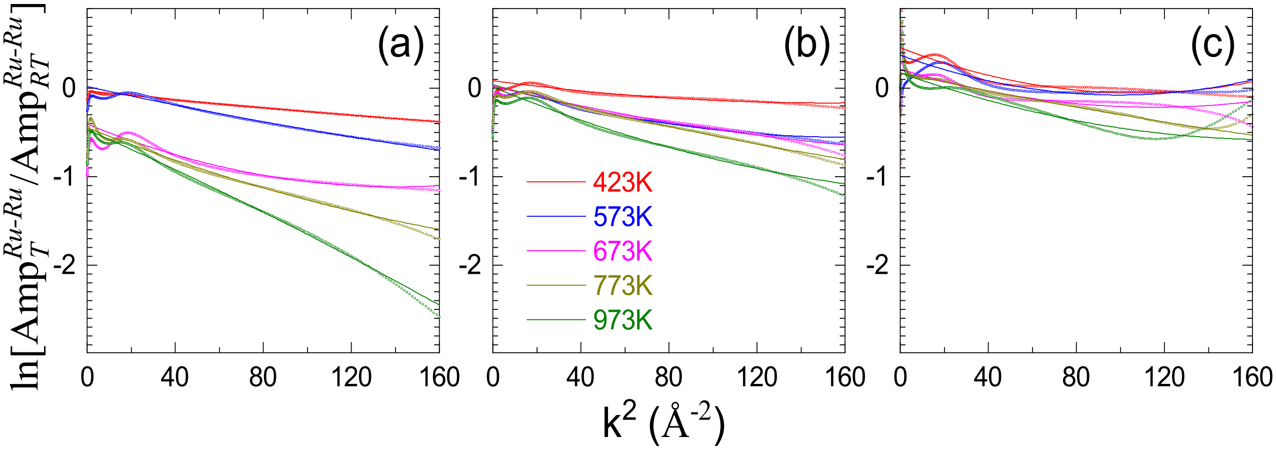

Figure 5: Log ratio plot and fits of Ru NPs (a), PdRu NPs (b) and PdRuIr NPs (c) measured at Ru K-edge at indicated temperatures.

For the present sample using the ratio approach, the variation of the temperature dependence of the Debye–Waller factor and coordination number was investigated on the Ru NPs, PdRu NPs, and PdRuIr NPs measured at the Ru K-edge, as shown in Figure 5. For the Ru NPs, the region covering the first FT peak between 1.7 and 3 Å was back Fourier transformed to obtain the χ(k) amplitude of the first Ru–Ru shell, which is an average of those of the Ru–Ru shell at 2.66 Å and 2.70 Å. Fig. 5(a) shows that up to 573 K, only the slope of the line increased, whereas at 673 K, there was a sudden decrease in the amplitude. After 673 K, the slope of the line further increased with temperature, indicating that at higher temperature, the disorder in the NPs is enhanced. Following a similar process for the PdRu NPs, one can see that the only effect of the temperature was enhancing the disorder. For the PdRuIr NPs, it is difficult to obtain the χ(k) amplitude by simply performing back Fourier transform around the first FT peak because this region of the FT spectrum covers the Ru–Ru and Ru–Ir shell of two distinct atomic pairs with some PVP adsorbed layer, which was simulated as a Ru–O shell owing to the similar shell distance of Ru–C and backscattering amplitude and phase shift. Therefore, to obtain the amplitude of the Ru–Ru shell, the FT spectrum measured at ambient temperature was fitted with the Ru–Ru, Ru–Ir, and Ru–O shell. The obtained metrical parameters for the Ru–Ru and Ru–Ir shell were kept fixed to fit the temperature-dependent FT spectra except for the atomic pair distance. The atomic pair distance was expected to change with temperature because of thermal expansion. The effect of the Debye–Waller factor was not removed from the temperature-dependent data by keeping σ fixed in the fitting. The Ru–Ru $\chi(\mathrm{k})$ component was later separated by subtracting the Ru–Ir and Ru–O components, and log ratio of the Ru–Ru shell was than obtained, as shown in Figure 5 (c). The relative changes in the intercept and slope were small in the PdRuIr samples compared with those for the Ru and PdRu NPs. This investigation revealed that in the Ru NPs, 673 K was the transition temperature at which the conversion of RuO_2 to RuO_4 occurred, leading to the earlier evaporation of Ru. In contrast, with the Pd and Ir doping, the formation of alloy phases reduced the probability of the formation of RuO_4 oxide, leading to the suppression of Ru evaporation. This suppression was observed to gradually increase with Pd and PdIr doping. Moreover, the advantage of adding these alloying elements on the catalytic properties signifies that these materials can be suited for TWC application and simultaneously show enhanced thermal stability.

Conclusions

The thermal stability and detailed local structure of newly synthesized PdRuIr NPs were investigated because of their better catalytic application, and a comparison was performed with Ru NPs and PdRu NPs, which exhibited poor thermal stability because of the evaporation of Ru at moderate temperatures. The local structure investigation revealed that in the PdRuIr NPs, Ir forms a solid-solution alloy with Ru and Pd. CCWT analysis showed that the RuIr alloys may crystallize into a novel fcc structure. The thermal stability of the alloy NPs was investigated by annealing from RT to 1273 K. XANES measurement revealed that the edge position and intensity of the near-edge feature showed abrupt changes for the Ru NPs at 673 K, whereas this sudden change was not observed for the PdRuIr NPs and the PdRu NPs showed slight improvement compared with the Ru NPs. The observed results were explained in terms of a dynamical fluctuation model. The dynamical fluctuation was attributed to the combined phenomenon of NP charging, chemical shift, and entropic effect. In the Ru NPs, the dynamical fluctuation plays a dominant role in the conversion of adsorbed O_2 to the volatile RuO_4 phase, resulting in the earlier evaporation of Ru. In the alloying phase, the dynamical fluctuation suppressed the formation of the RuO_4 phase, which eventually helped to enhance the thermal stability of the PdRuIr NPs.

Supporting Information

Figure S1: Comparison of Pd K-edge EXAFS of PdRu and PdRuIr NPs.

Figure S2: CCWT spectra of Ru NPs and PdRu NPs.

Figure S3: CCWT spectra of bulk Ru and Pd.

Figure S4: XRD data of Ru NPs, Pd NPs, Ir NPs, and PdRuIr NPs.

Figure S5: Comparison of XANES spectra at different temperatures for Ru NPs, PdRu NPs, and PdRuIr NPs.

Section describing synthesis process of the nanoparticles.

Acknowledgements

The experiments were measured at SPring-8 under proposal Nos. 2018B1018, 2018B1143, 2019A1002, 2019B1271, 2019B1278, 2020A1141, and 2020A1142. This project is partially funded by ACCEL (JPMJAC1501) and the Japan Society for the Promotion of Science (JSPS) KAKENHI No. 18K04868 and 20K15083. The authors would also like to thank Tiffany Jain, M.S., from Edanz Group (https://en-author-services.edanz.com/ac) for editing

a draft of this manuscript.

References

(1) Assmann, J.; Narkhede, V.; Khodeir, L.; Löffler, E.; Hinrichsen, O.; Birkner, A.; Over, H.; Muhler, M. On the Nature of the Active State of Supported Ruthenium Catalysts Used for the Oxidation of Carbon Monoxide: Steady-State and Transient Kinetics Combined with in Situ Infrared Spectroscopy. *J. Phys. Chem. B* **2004**, *108*, 14634–14642, DOI: `10.1021/jp0401675`.

(2) Bowker, M. Automotive Catalysis Studied by Surface Science. *Chem. Soc. Rev.* **2008**, *37*, 2204–2211, DOI: `10.1039/B719206C`.

(3) Joo, S. H.; Park, J. Y.; Renzas, J. R.; Butcher, D. R.; Huang, W.; Somorjai, G. A. Size Effect of Ruthenium Nanoparticles in Catalytic Carbon Monoxide Oxidation. *Nano Lett.* **2010**, *10*, 2709–2713, DOI: `10.1021/nl101700j`.

(4) Perkas, N.; Teo, J.; Shen, S.; Wang, Z.; Highfield, J.; Zhong, Z.; Gedanken, A. Supported Ru Catalysts Prepared by two Sonication-Assisted Methods for Preferential Oxidation of CO in H_2. *Phys. Chem. Chem. Phys.* **2011**, *13*, 15690–15698, DOI: `10.1039/C1CP21870K`.

(5) Iost, K. N.; Borisov, V. A.; Temerev, V. L.; Surovikin, Y. V.; Pavluchenko, P. E.; Trenikhin, M. V.; Lupanova, A. A.; Arbuzov, A. B.; Shlyapin, D. A.; Tsyrulnikov, P. G., et al. Study on the Metal-Support Interaction in the Ru/C Catalysts Under Reductive Conditions. *Surf. Interfaces* **2018**, *12*, 95–101, DOI: `https://doi.org/10.1016/j.surfin.2018.05.003`.

(6) Wu, D.; Kusada, K.; Kitagawa, H. Recent Progress in the Structure Control of Pd-Ru Bimetallic Manomaterials. *Sci. Technol. Adv. Mater.* **2016**, *17*, 583–596, DOI: `10.1080/14686996.2016.1221727`.

(7) Kusada, K.; Kobayashi, H.; Ikeda, R.; Kubota, Y.; Takata, M.; Toh, S.; Yamamoto, T.; Matsumura, S.; Sumi, N.; Sato, K., et al. Solid Solution Alloy Nanoparticles of Immiscible Pd and Ru Elements Neighboring on Rh: Changeover of the Thermodynamic Behavior for Hydrogen Storage and Enhanced CO-Oxidizing Ability. *J. Am. Chem. Soc.* **2014**, *136*, 1864–1871, DOI: `10.1021/ja409464g`.

(8) Sato, K.; Tomonaga, H.; Yamamoto, T.; Matsumura, S.; Zulkifli, N. D. B.; Ishimoto, T.; Koyama, M.; Kusada, K.; Kobayashi, H.; Kitagawa, H., et al. A Synthetic Pseudo-Rh: NO_x Reduction Activity and Electronic Structure of Pd-Ru Solid-solution Alloy Nanoparticles. *Sci. Rep.* **2016**, *6*, 28265, DOI: `10.1038/srep28265`.

(9) Song, C.; Tayal, A.; Seo, O.; Kim, J.; Chen, Y.; Hiroi, S.; Kumara, L. S. R.; Kusada, K.; Kobayashi, H.; Kitagawa, H., et al. Correlation Between the Electronic/Local Structure and CO-oxidation Activity of Pd_xRu_{1-x} Alloy Nanoparticles. *Nanoscale Adv.* **2019**, *1*, 546–553, DOI: `10.1039/C8NA00305J`.

(10) Xiao, S.; Hu, W.; Luo, W.; Wu, Y.; Li, X.; Deng, H. Size Effect on Alloying Ability and Phase Stability of Immiscible Bimetallic Nanoparticles. *Eur. Phys. J. B - Condens. Matter Complex Syst.* **2006**, *54*, 479–484, DOI: `10.1140/epjb/e2007-00018-6`.

(11) Tayal, A.; Seo, O.; Kim, J.; Kumara, L. S. R.; Song, C.; Hiroi, S.; Chen, Y.; Kobayashi, H.; Kitagawa, H.; Sakata, O. Effects of Interfacial Structure of Pd-Pt Nanoparticles on Hydrogen Solubility. *J. Alloys Compd.* **2019**, *791*, 1263–1269, DOI: `https://doi.org/10.1016/j.jallcom.2019.03.342`.

(12) Xiao, L.; Zhuang, L.; Liu, Y.; Lu, J.; Héctor, D. A. Activating Pd by Morphology Tailoring for Oxygen Reduction. *J. Am. Chem. Soc.* **2009**, *131*, 602–608, DOI: `10.1021/ja8063765`.

(13) Newton, M. A.; Belver-Coldeira, C.; Martínez-Arias, A.; Fernández-García, M. Dy-

namic in situ Observation of Rapid Size and Shape Change of Supported Pd Nanoparticles during CO/NO Cycling. *Nat. Mater.* **2007**, *6*, 528, DOI: `10.1038/nmat1924`.

(14) Kusada, K.; Wu, D.; Nanba, Y.; Koyama, M.; Yamamoto, T.; Tran, X. Q.; Toriyama, T.; Matsumura, S.; Ito, A.; Sato, K., et al. Highly Stable and Active Solid-Solution-Alloy Three-Way Catalyst by Utilizing Configurational-Entropy Effect. *Adv. Mater.* **2021**, *33*, 2005206, DOI: `https://doi.org/10.1002/adma.202005206`.

(15) Kusada, K.; Wu, D.; Nanba, Y.; Koyama, M.; Yamamoto, T.; Tran, X. Q.; Toriyama, T.; Matsumura, S.; Ito, A.; Sato, K., et al. Catalysts for Gas Purification: Highly Stable and Active Solid-Solution-Alloy Three-Way Catalyst by Utilizing Configurational-Entropy Effect. *Adv. Mater.* **2021**, *33*, 2170120, DOI: `https://doi.org/10.1002/adma.202170120`.

(16) van Bokhoven, J. A.; Miller, J. T. d Electron Density and Reactivity of the d Band as a Function of Particle Size in Supported Gold Catalysts. *J. Phys. Chem. C* **2007**, *111*, 9245–9249, DOI: `10.1021/jp070755t`.

(17) Okal, J.; Zawadzki, M.; Tylus, W. Microstructure Characterization and Propane Oxidation over Supported Ru Nanoparticles Synthesized by the Microwave-Polyol Method. *Appl. Catal. B: Environ.* **2011**, *101*, 548 – 559, DOI: `https://doi.org/10.1016/j.apcatb.2010.10.028`.

(18) Liu, X.; Wang, D.; Li, Y. Synthesis and Catalytic Properties of Bimetallic Nanomaterials with Various Architectures. *Nano Today* **2012**, *7*, 448 – 466, DOI: `https://doi.org/10.1016/j.nantod.2012.08.003`.

(19) Stonkus, O. A.; Kibis, L. S.; Yu. Podyacheva, O.; Slavinskaya, E. M.; Zaikovskii, V. I.; Hassan, A. H.; Hampel, S.; Leonhardt, A.; Ismagilov, Z. R.; Noskov, A. S., et al. Palladium Nanoparticles Supported on Nitrogen-Doped Carbon Nanofibers: Synthesis, Microstructure, Catalytic Properties, and Self-Sustained Oscillation Phenom-

ena in Carbon Monoxide Oxidation. *ChemCatChem* **2014**, *6*, 2115–2128, DOI: `10.1002/cctc.201402108`.

(20) Ravel, B.; Newville, M. *ATHENA*, *ARTEMIS*, *HEPHAESTUS*: Data Analysis for X-ray Absorption Spectroscopy using *IFEFFIT*. *J. Synchrotron Radiat.* **2005**, *12*, 537–541, DOI: `10.1107/S0909049505012719`.

(21) Teo, B. K., Joy, D. C., Eds. *EXAFS Spectroscopy: Techniques and Applications*; Springer: US, 1981.

(22) Conradson, S. D.; Durakiewicz, T.; Espinosa-Faller, F. J.; An, Y. Q.; Andersson, D. A.; Bishop, A. R.; Boland, K. S.; Bradley, J. A.; Byler, D. D.; Clark, D. L., et al. Possible Bose-Condensate Behavior in a Quantum Phase Originating in a Collective Excitation in the Chemically and Optically Doped Mott-Hubbard System UO_{2+x}. *Phys. Rev. B* **2013**, *88*, 115135, DOI: `10.1103/PhysRevB.88.115135`.

(23) Gao, M.; Zhang, C.; Gao, P.; Zhang, F.; Ouyang, L.; Widom, M.; Hawk, J. Thermodynamics of Concentrated Solid Solution Alloys. *Curr. Opin. Solid State Mater. Sci.* **2017**, *21*, 238–251, DOI: `https://doi.org/10.1016/j.cossms.2017.08.001`.

(24) Galsin, J. S. *Solid State Phys.*; Academic Press, 2020; p 656, DOI: `https://doi.org/10.1016/C2018-0-01175-5`.

(25) Miyajima, K.; Fukushima, N.; Himeno, H.; Yamada, A.; Mafuné, F. Breakdown of the Hume-Rothery Rules in Sub-Nanometer-Sized Ta-Containing Bimetallic Small Clusters. *J. Phys. Chem. A* **2009**, *113*, 13448–13450, DOI: `10.1021/jp908415y`.

(26) Kusada, K.; Kobayashi, H.; Yamamoto, T.; Matsumura, S.; Sumi, N.; Sato, K.; Nagaoka, K.; Kubota, Y.; Kitagawa, H. Discovery of Face-Centered-Cubic Ruthenium Nanoparticles: Facile Size-Controlled Synthesis Using the Chemical Reduction Method. *J. Am. Chem. Soc.* **2013**, *135*, 5493–5496, DOI: `10.1021/ja311261s`.

(27) Penner-Hahn, J. In *Comprehensive Coord. Chem. II*; McCleverty, J. A., Meyer, T. J., Eds.; Pergamon: Oxford, 2003; pp 159–186, DOI: `https://doi.org/10.1016/B0-08-043748-6/01063-X`.

(28) Frenkel, A. I.; Yevick, A.; Cooper, C.; Vasic, R. Modeling the Structure and Composition of Nanoparticles by Extended X-Ray Absorption Fine-Structure Spectroscopy. *Annu. Rev. Anal. Chem.* **2011**, *4*, 23–39, DOI: `10.1146/annurev-anchem-061010-113906`.

(29) Marinković, N. S.; Sasaki, K.; Adžić, R. R. Nanoparticle Size Evaluation of Catalysts by EXAFS: Advantages and Limitations. *Zaštita Materijala* **2016**, *57*, 101–109, DOI: `10.5937/ZasMat1601101M`.

(30) Munõz, M.; Argoul, P.; Farges, F. Continuous Cauchy Wavelet Transform Analyses of EXAFS Spectra: A Qualitative Approach. *Am. Mineral.* **2003**, *88*, 694, DOI: `10.2138/am-2003-0423`.

(31) Andreazza, P.; Khelfane, H.; Lyon, O.; Andreazza-Vignolle, C.; Ramos, A. Y.; Samah, M. Trends in Aanomalous Small-Angle X-ray Scattering in Grazing Incidence for Supported Nanoalloyed and Core-Shell Metallic Nanoparticles. *Eur. Phys. J. Special Top.* **2012**, *208*, 231–244, DOI: `10.1140/epjst/e2012-01621-4`.

(32) Kostroun, V. O.; Fairchild, R. W.; Kukkonen, C. A.; Wilkins, J. W. Systematic Structure in the K-edge Photoabsorption Spectra of the 4d Transition Metals. *Phys. Rev. B* **1976**, *13*, 3268–3271, DOI: `10.1103/PhysRevB.13.3268`.

(33) Muller, J. E.; Jepsen, O.; Andersen, O. K.; Wilkins, J. W. Systematic Structure in the K-Edge Photoabsorption Spectra of the 4d Transition Metals: Theory. *Phys. Rev. Lett.* **1978**, *40*, 720–722, DOI: `10.1103/PhysRevLett.40.720`.

(34) Nilsson, J.; Carlsson, P.-A.; Grönbeck, H.; Skoglundh, M. First Principles Calcula-

tions of Palladium Nanoparticle XANES Spectra. *Top. Catal.* **2017**, *60*, 283–288, DOI: `10.1007/s11244-016-0612-0`.

(35) Zhu, X.; Guo, Q.; Sun, Y.; Chen, S.; Wang, J.-Q.; Wu, M.; Fu, W.; Tang, Y.; Duan, X.; Chen, D., et al. Optimising Surface d Charge of AuPd Nanoalloy Catalysts for Enhanced Catalytic Activity. *Nat. Comm.* **2019**, *10*, 1428, DOI: `10.1038/s41467-019-09421-5`.

(36) Vila, F.; Rehr, J. J.; Kas, J.; Nuzzo, R. G.; Frenkel, A. I. Dynamic Structure in Supported Pt Nanoclusters: Real-time Density Functional Theory and X-ray Spectroscopy Simulations. *Phys. Rev. B* **2008**, *78*, 121404, DOI: `10.1103/PhysRevB.78.121404`.

(37) Frenkel, A. I.; Hills, C. W.; Nuzzo, R. G. A View from the Inside: Complexity in the Atomic Scale Ordering of Supported Metal Nanoparticles. *J. Phys. Chem. B* **2001**, *105*, 12689–12703, DOI: `10.1021/jp012769j`.

(38) Bunker, G. Application of the Ratio Method of EXAFS Analysis to Disordered Systems. *Nucl. Instrum. Methods Phys. Res.* **1983**, *207*, 437–444, DOI: `https://doi.org/10.1016/0167-5087(83)90655-5`.

(39) Clausen, B. S.; Nørskov, J. K. Asymmetric Pair Distribution Functions in Catalysts. *Top. Catal.* **2000**, *10*, 221–230, DOI: `10.1023/A:1019196908404`.

(40) Calvin, S. *XAFS for Everyone*; CRC press, 2013; p 457.

TOC Graphic

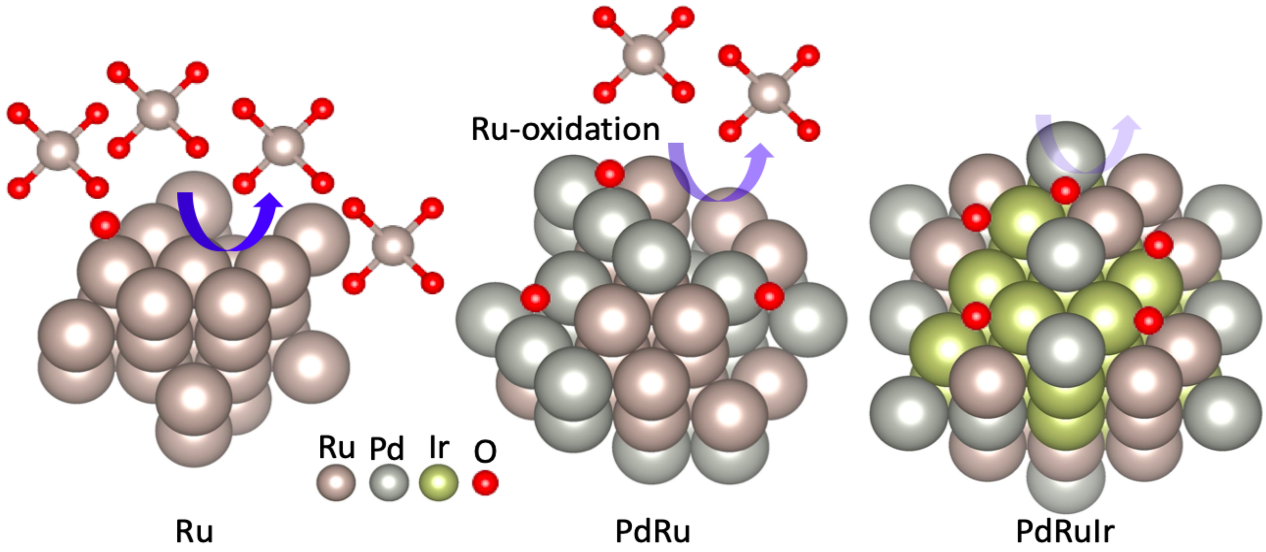

Figure 6